Available online at www.sciencedirect.com
ScienceDirect
Journal of Power Sources 180 (2008) 506–515
JOURNAL OF POWER SOURCES
www.elsevier.com/locate/jpowsour

Improved configuration of supported nickel catalysts in a steam reformer for effective hydrogen production from methane

Shinku Lee, Joongmyeon Bae *, Sungkwang Lim, Joonguen Park

Department of Mechanical Engineering, School of Mechanical, Aerospace & Systems Engineering, Republic of Korea

Received 10 October 2007; received in revised form 14 January 2008; accepted 24 January 2008
Available online 14 February 2008

Abstract

The heat and mass transfer characteristics in a steam reformer are investigated via experimental and numerical approaches and a new configuration of packed catalysts is proposed for effective hydrogen production. Prior to the numerical investigation, parametric studies are carried for the furnace temperature, steam-to-carbon (S:C) ratio, and gas flow rate. After validation of the developed code, numerical work is undertaken to determine the relationship of the operating parameters. Based on the experimental and numerical results, and with the goal of obtaining optimum heat transfer characteristics and an efficient catalyst array, a new configuration for the packed bed is proposed and numerically investigated taking into account the endothermicity of the steam reforming reaction. A bed packed repeatedly with inert and active catalysts is found to be an efficient means to obtain the same, or better, hydrogen production with small amounts of the active catalysts compared with a typical steam reformer.

Keywords: Steam reforming; Reactor modelling; Hydrogen; Improved catalyst packing; Methane; Fuel cell

1. Introduction

Offering high energy-conversion efficiency and low emission of air pollutants, the fuel cell holds promise for application as an energy source. The various types of fuel cell developed to date are operated with hydrogen [1–3]. For successful commercialization, a stable supply of hydrogen is required at low cost and with high efficiency [4]. There are many technologies to produce hydrogen from hydrocarbons [5–7]. Among these technologies, industrial steam reforming (SR) reactors with various types of burner have been widely studied. Although they have a strong endothermic nature, SR reactors deliver a high hydrogen yield [4,8]. There are also various technologies to supply the necessary reaction heat in an efficient manner.

Basic SR reactor designs vary according to the arrangement of the burners, namely top-fired, bottom-fired, side-fired and terrace wall types. Different tube wall temperatures and heat flux profiles can be observed according to the position of the burners [9]. Tubes packed with supported nickel catalysts should be selected rigorously due to material issues related to exposure at high temperatures. In addition, the large amount of heat supply and the endothermic reforming reactions cause significant axial and radial temperature gradients in the reformer. These phenomena affect the performance of the reformer, especially in the central region, because of heat transfer limitations. Since combustion is controlled via dilution with excess air, the material problem can be solved. Basically, the temperature at the tube wall should be maintained at a value that is as low as possible in order to extend the tube lifetime [10,11]. To compensate for shortcomings such as reduction in the lifetime of the tube, various approaches have been reported, including distribution of active catalysts and optimization of heat flux profiles [12,13].

Reactor analysis and design are necessary in order to develop different catalyst arrangements for high efficiency and long-term stability with optimized heat transfer. To this end, a Langmuir–Hinshelwood type of heterogeneous reaction model may be adequate for analyzing the heat and mass transfer characteristics between bulk gas and catalysts, instead of the pseudo-homogeneous model [14]. In addition, an effectiveness factor could be used to take into account

* Corresponding author at: Department of Mechanical Engineering, School of Mechanical, Aerospace & Systems Engineering, Korea Advanced Institute of Science and Technology, 335 Gwahangno, Yuseong-gu, Daejeon 305-701, Republic of Korea. Tel.: +82 42 869 3045; fax: +82 42 869 3210.
E-mail address: jmbae@kaist.ac.kr (J. Bae).

0378-7753/$ – see front matter © 2008 Elsevier B.V. All rights reserved.
doi:10.1016/j.jpowsour.2008.01.081

Nomenclature

a_{sf}	interfacial surface area (m^{-1})
C_p	heat capacity ($J\,kg^{-1}\,K^{-1}$)
D	diffusivity ($m^2\,s^{-1}$)
E	activation energy ($kJ\,kmol^{-1}$)
h	heat transfer coefficient/mass transfer coefficient ($W\,m^{-2}\,K^{-1}$) or ($m\,s^{-1}$)
k	thermal conductivity ($W\,m^{-1}\,s^{-1}$)
K	permeability (m^2)
p	pressure ($N\,m^{-2}$)
q''	heat flux ($W\,m^{-2}$)
r	radial coordinate of the reactor (m)
R	Universal gas constant ($8.314\,J\,mol^{-1}\,K^{-1}$)
t	time (s)
T	temperature (K)
u	axial velocity ($m\,s^{-1}$)
v	radial velocity ($m\,s^{-1}$)
W	molecular weight ($kg\,kmol^{-1}$)
Y	mass fraction
z	axial coordinate of the reactor (m)

Greek symbols

ε	porosity
η	effectiveness factor
μ	dynamic viscosity ($kg\,s^{-1}\,m^{-1}$)
ρ	density ($kg\,m^{-3}$)

Superscript

in	inlet

Subscripts

c	centerline of the reactor
cat	catalyst
d	mass
D	Darcian
eff	effective
f	fluid phase
s	solid phase
t	heat
w	wall

the significant reduction of reaction kinetics due to intra-particle mass-transport limitations [15]. In this study, heat and mass transfer phenomena are extensively analyzed using a heterogeneous two-dimensional model with experimental and numerical approaches. Due to heat transfer characteristics and low residence time for chemical species participating in the reactions, hydrogen production at high reactant flow rate is remarkably decreased. Improved configurations of the catalytic bed that entail repeated inert and active catalyst packing are introduced with the aim of mitigating the heat transfer limitation.

2. Experiments

2.1. Experimental set-up

A schematic diagram of the SR experimental set-up is presented in Fig. 1. A fixed-bed reactor is located in an electrical furnace. Air, fuel and water are fed as a mixture into the reactor while the temperature is controlled by a furnace. Water is vapourized by an external heat-exchanger and supplied to the reactor. The reactor is a stainless-steel tubular bed (inner diameter = 15.7 mm, length = 126 mm) that is filled with nickel catalyst supported on alumina; the tube is 0.5-mm thick. Reactor temperatures are measured and monitored continuously at eight points along its centre line by means of K-type thermocouples. Temperatures at the outer wall of the reactor are also measured at several locations. Pipelines that connect the evaporator and the reactor are heated electrically to prevent steam condensation. The flow rates of methane, nitrogen and air are controlled by mass-flow controllers (MFCs), and the flow rate of water is controlled by a high-performance liquid chromatograph (HPLC) pump. Moisture in the product gases is removed by a chiller and a silica gel trap for analyses of gaseous compositions. Dry product gases are analyzed with an Agilent 6890 gas chromatograph (GC) using a thermal conductivity detector (TCD) and a flame ionization detector (FID). H_2, CO, CO_2, and N_2 are detected by the TCD with argon as a carrier gas, and all hydrocarbons are detected by the FID with helium as a carrier gas.

2.2. Experimental results

In the present experiment, the influence of the furnace temperature and the steam-to-carbon (S:C) ratio are assessed with an average catalyst pellet size of 250–425 μm to exclude the effect of catalyst shape. Additionally, heat transfer and diffusion limitations are studied with different volume flow rates of the feedstock. To take the diffusion limitation into account, 3-mm spherical catalysts are used.

In order to investigate the characteristics of commercial catalysts, the furnace temperature is varied. Fig. 2 shows the variation in the composition of the production gas with furnace tempera-

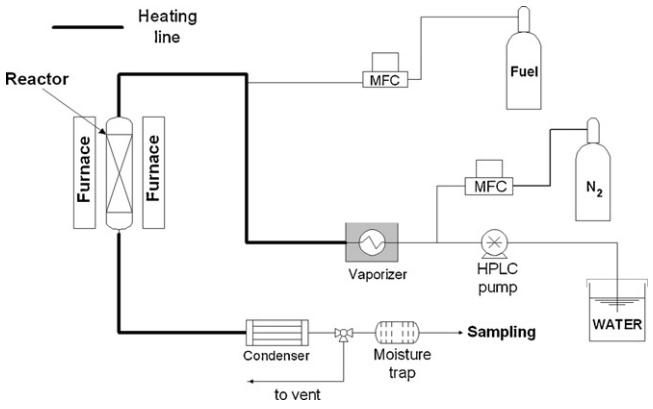

Fig. 1. Schematic of experimental setup.

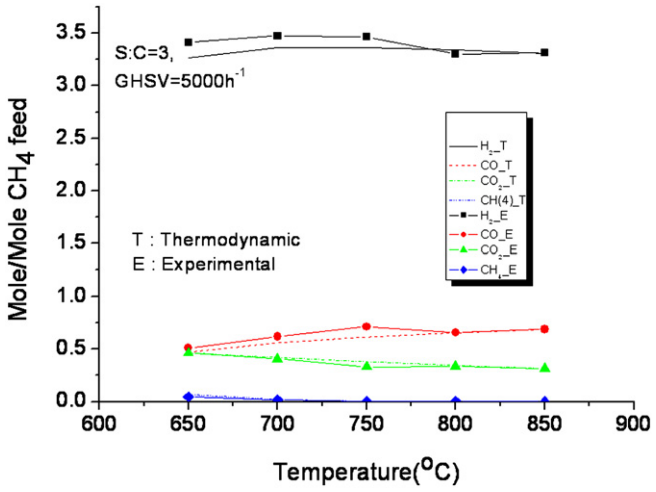

Fig. 2. Product gas concentrations vs. furnace temperature (S:C = 3, GHSV = 5000 h^{-1}).

ture. The gas hourly space velocity (GHSV) is defined as

$$\text{GHSV}\,(h^{-1}) = \frac{\text{volume flow rate of feedstock}}{\text{volume of catalyst bed}} \quad (1)$$

In this case, GHSV is 5000 h^{-1} and the S:C ratio is fixed at 3.0. In Fig. 2, hydrogen production tends to be higher and follows the equilibrium composition of the species as the temperature is increased. High temperature is favourable for the reaction, but energy input is proportional to the reaction temperature. Based on the thermodynamic equilibrium, hydrogen production is highest at around 700 °C under the given operating conditions. The variance in hydrogen production, however, is negligible when the temperature is above 700 °C.

The influence of the S:C ratio was investigated at 850 °C, at which GHSV is 5000 h^{-1}. As expected, a higher S:C ratio results in higher hydrogen yield, as shown in Fig. 3. The temperature is sufficient to give a higher hydrogen yield with respect to injected methane.

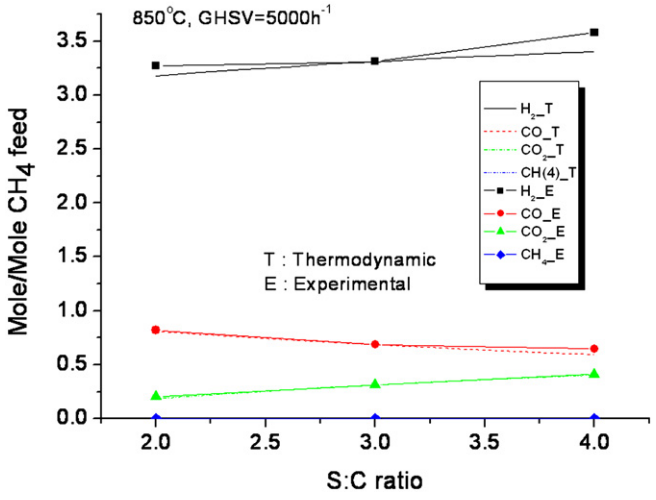

Fig. 3. Product gas concentrations vs. S:C ratio (furnace temperature = 850 °C, GHSV = 5000 h^{-1}).

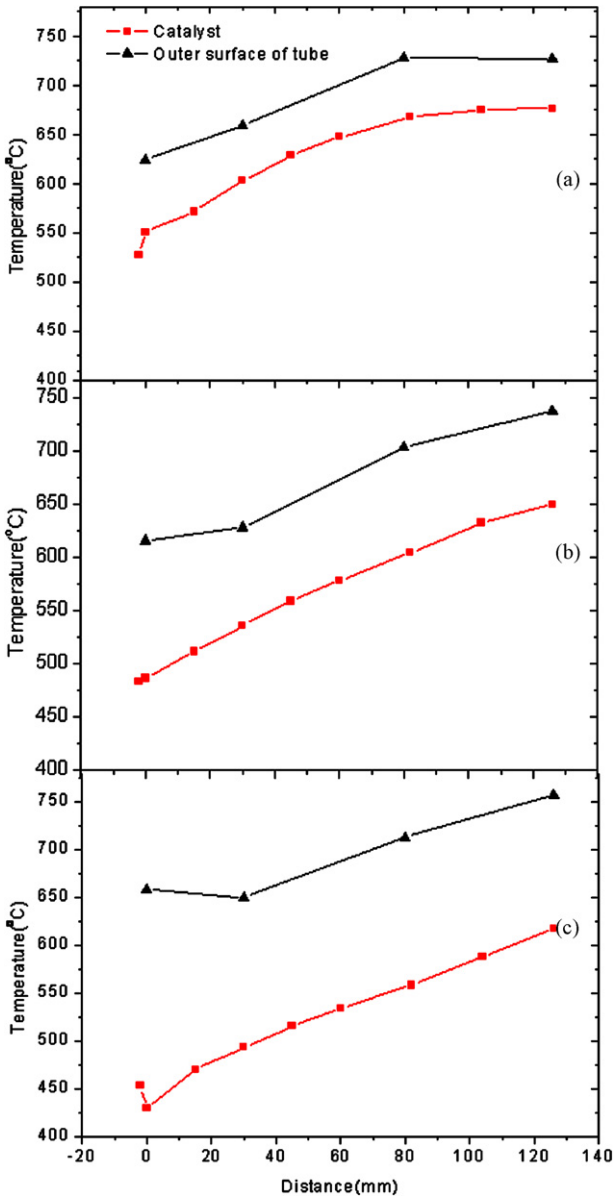

Fig. 4. (a) Temperature distribution of catalyst and outer wall (furnace temperature = 700 °C, GHSV = 2500 h^{-1}, S:C = 3). (b) Temperature distribution of catalyst and outer wall (furnace temperature = 700 °C, GHSV = 5000 h^{-1}, S:C = 3). (c) Temperature distribution of catalyst and outer wall (furnace temperature = 750 °C, GHSV = 10,000 h^{-1}, S:C = 3).

Finally, in order to determine the effect of heat transfer, a spherical nickel alumina catalyst with a size of 3 mm and 10% active metal was packed into the bed. Fig. 4(a–c) report temperature profiles of the catalyst and the outer wall at different GHSVs. From the results, it is found that the temperature difference between the catalyst and outer wall increases markedly as GHSV increases. Heat transfer limitation and short residence time degrade the performance of the SR reactor in the high GHSV region. A more detailed discussion of this behaviour is presented below in Section 3.6

3. Mathematical formulation

3.1. Governing equations

In this section, mathematical governing equations are introduced in order to describe the physical phenomena in the steam reformer. Mass, momentum, energy and species equations are solved simultaneously and include the catalytic reaction on the surface. In the porous medium, permeability is a key parameter to estimate the pressure drop in the flow. For a more rigorous analysis, permeability is determined by the lattice Boltzmann method [16].

For the chemical reaction on the surface of the supported nickel catalyst, the Langmuir–Hinshelwood model is incorporated, assuming that this reaction is the rate-determining step. All the governing equations are formulated in an axisymmetric coordinates system. For the energy equation, a heterogeneous model of gaseous species and solid catalyst particles is employed to consider thermally non-equilibrium phenomena. The equations are as follows:

$$\frac{\partial \rho_f}{\partial t} + \frac{\partial}{\partial z}(\rho_f u_D) + \frac{1}{r}\frac{\partial}{\partial r}(r\rho_f v_D) = 0 \tag{2}$$

where the subscript D denotes the Darcian velocity.

$$\frac{\partial \rho_f u_D}{\partial t} + \frac{\partial}{\partial z}(\rho_f u_D u_D) + \frac{1}{r}\frac{\partial}{\partial r}(r\rho_f u_D v_D) = -\frac{\partial p}{\partial z} + \frac{\partial}{\partial z}\left(\mu_{eff}\frac{\partial u_D}{\partial z}\right) + \frac{1}{r}\frac{\partial}{\partial r}\left(r\mu_{eff}\frac{\partial u_D}{\partial r}\right) - \frac{\mu}{K}u_D \tag{3a}$$

$$\frac{\partial \rho_f v_D}{\partial t} + \frac{\partial}{\partial z}(\rho_f u_D v_D) + \frac{1}{r}\frac{\partial}{\partial r}(r\rho_f v_D v_D) = -\frac{\partial p}{\partial r} + \frac{\partial}{\partial z}\left(\mu_{eff}\frac{\partial v_D}{\partial z}\right) + \frac{1}{r}\frac{\partial}{\partial r}\left(r\mu_{eff}\frac{\partial v_D}{\partial r}\right) - \frac{\mu}{K}v_D \tag{3b}$$

where K denotes the permeability.

$$\frac{\partial(\varepsilon\rho_f C_{p,f} T_f)}{\partial t} + \frac{\partial}{\partial z}(\rho_f C_{p,f} u_D T_f) + \frac{1}{r}\frac{\partial}{\partial r}(r\rho_f C_{p,f} v_D T_f) = \frac{\partial}{\partial z}\left(k_{eff,f}\frac{\partial T_f}{\partial z}\right) + \frac{1}{r}\frac{\partial}{\partial r}\left(r k_{eff,f}\frac{\partial T_f}{\partial r}\right) + h_t a_{t,sf}(T_s - T_f) \tag{4}$$

where $k_{eff,f}$ denotes the effective thermal conductivity for bulk gas.

$$\frac{\partial((1-\varepsilon)\rho_s C_{p,s} T_s)}{\partial t} = \frac{\partial}{\partial z}\left(k_{eff,s}\frac{\partial T_s}{\partial z}\right) + \frac{1}{r}\frac{\partial}{\partial r}\left(r k_{eff,s}\frac{\partial T_s}{\partial r}\right) + h_t a_{t,sf}(T_f - T_s) + \rho_{cat}\sum_{j=1}^{N}(-\Delta H_j)\eta_j R_j \tag{5}$$

where $k_{eff,s}$ denotes the effective thermal conductivity for the catalyst.

$$\frac{\partial(\varepsilon\rho_f Y_f)}{\partial t} + \frac{\partial}{\partial z}(\rho u_D Y_f) + \frac{1}{r}\frac{\partial}{\partial r}(r\rho v_D Y_f) = \frac{\partial}{\partial z}\left(D_{eff}\frac{\partial \rho_f Y_f}{\partial z}\right) + \frac{1}{r}\frac{\partial}{\partial r}\left(r D_{eff}\frac{\partial \rho_f Y_f}{\partial r}\right) + \rho_f h_d a_{d,sf}(Y_s - Y_f) \tag{6}$$

where Y is the mass fraction of species.

$$\frac{\partial((1-\varepsilon)\rho_f Y_s)}{\partial t} = \rho_f h_d a_{d,sf}(Y_f - Y_s) + \rho_{cat} r_i M_i \tag{7}$$

where r_i represents the conversion rates of the individual species.

3.2. Boundary conditions

For simplicity of the given problems, the transient term is omitted. Hence, only the boundary conditions, except the initial, condition, are implemented to obtain the solutions, as follows:

(a) At the reformer inlet face: $z = 0$

$$T_f = T_f^{in}; \qquad \frac{\partial T_s}{\partial z} = 0; \qquad Y_f = Y_f^{in} \tag{8}$$

(b) At the reformer outlet face: $z = L$

$$\frac{\partial T_f}{\partial z} = 0; \qquad \frac{\partial T_s}{\partial z} = 0; \qquad \frac{\partial Y_f}{\partial z} = 0 \tag{9}$$

(c) At the reformer centre: $r = 0$

$$\frac{\partial T_f}{\partial r} = 0; \qquad \frac{\partial Y_f}{\partial r} = 0 \tag{10}$$

(d) At the interfacial surface of the inner reformer wall and the catalyst bed: $r = R$

$$-k_{eff,f}\frac{\partial T_f}{\partial r} - k_{eff,s}\frac{\partial T_s}{\partial r} = q''(z); \quad T_f = T_s \tag{11a}$$

$$T_f = T_s = T(z) \tag{11b}$$

$$\frac{\partial Y_f}{\partial r} = 0 \tag{11c}$$

Two different boundary conditions are implemented for the energy equation. Eq. (11a) is used for the heat flux condition, and Eq. (11b) is used for the specified reformer wall temperature.

3.3. Constitutive equations

In order to solve the established governing equations, some supplementary relations are first introduced in this section. Since the SR reaction takes place in porous media, all the physical parameters should be modelled in this region. Permeability can be determined by the following correlation, for which the lattice Boltzmann method is used, as follows:

$$\frac{K}{D^2} = \exp\{C_1 \ln\left(\frac{\varepsilon^{11/3}}{(1-\varepsilon)^2}\right) - C_2\} \tag{12}$$

where D is the characteristic length of packed materials and the coefficients C_1 and C_2 are dependent upon Kn_o, which has the following correlations:

$$C_1 = 0.709 - 1.62Kn_o + 5.892Kn_o^2 \quad (13)$$

$$C_2 = 5.09 - 14.14Kn_o + 36.84Kn_o^2 \quad (14)$$

where Kn_o is the Knudsen number at the outlet.

In addition, the effective thermal conductivity for bulk gas and a solid can be determined by

$$k_{eff,f} = \varepsilon k_f; \qquad k_{eff,s} = (1-\varepsilon)k_s \quad (15)$$

Also, the properties of gases in the reformer are determined using Chapman–Enskog kinetic theory [17]. The overall properties such as density and heat capacity can be evaluated based on mole or mass fractions and bulk gas temperature. The bulk gas density is given by

$$\rho_f = \frac{p}{RT\sum_i Y_i/W_i} \quad (16)$$

The ideal gas law is incorporated for mixtures of gases.

Since a heterogeneous reaction model is incorporated in the present work, the heat transfer coefficient and interfacial surface area between the bulk gas and catalyst are significant determinants of reformer performance. The heat transfer coefficient between the catalyst and the gas is determined by the Reynolds number and Prandtl number. Correlation models have been presented in detail in the literature and are widely accepted [18]. The interfacial surface area between the bulk gas and the catalyst can be estimated from the BET surface area of the given catalyst. Physical variables for the simulation are shown in Table 1.

3.4. Chemical reaction

In this study, SR and water-gas shift (WGS) reaction for methane are simultaneously taken into account to analyze the performance of the reformer. The kinetic rate equations for the SR and WGS reactions are taken from a previous study [19].Three overall chemical reactions are adopted:

(i) the endothermic SR reaction to produce H_2 and CO:

$$CH_4 + H_2O \leftrightarrow CO + 3H_2$$
$$\Delta H_{1(298\,K)} = 206,000\,kJ\,kmol^{-1} \quad (17)$$

(ii) the WGS reaction:

$$CO + H_2O \leftrightarrow CO_2 + H_2$$
$$\Delta H_{2(298\,K)} = -41,000\,kJ\,kmol^{-1} \quad (18)$$

Table 1
Physical parameters for the simulation

Physical variables	Value
Inlet pressure (p^{in}) (bar)	1
Porosity (ε)	0.6
Interfacial surface area (a_{sf}) ($l\,m^{-1}$)	2000
Catalyst density (ρ_{cat}) ($kg\,m^{-3}$)	2000

Table 2
Kinetic parameters

Reaction	A_i ($kmol\,kg_{cat}^{-1}\,s^{-1}$)	E_i ($kJ\,mol^{-1}$)
1	$1.174 \times 10^{12}\,bar^{0.5}$	240.10
2	$5.43 \times 10^{2}\,bar^{-1}$	67.13
3	$2.83 \times 10^{11}\,bar^{0.5}$	243.90

(iii) the direct SR reaction to CO_2:

$$CH_4 + 2H_2O \leftrightarrow CO_2 + 3H_2,$$
$$\Delta H_{3(298\,K)} = 165,000\,kJ\,kmol^{-1} \quad (19)$$

The following kinetic rate equations are derived from the Langmuir–Hinshelwood model assuming the surface reaction is the slowest step among adsorption, surface reaction and desorption. The rate equations for methane [Eqs. (17)–(19)] can be expressed by

$$r_1 = k_1 \frac{p_{CH_4} p_{H_2O}/p_{H_2}^{2.5} - p_{CO}\,p_{H_2}^{0.5}/K_{p1}}{DEN^2} \quad (20)$$

$$r_2 = k_2 \frac{p_{CO}\,p_{H_2O}/p_{H_2} - p_{CO_2}/K_{p2}}{DEN^2} \quad (21)$$

$$r_3 = k_3 \frac{p_{CH_4}/p_{H_2}^{1.5} - p_{H_2}^{0.5}\,p_{CO_2}/K_{p3}}{DEN^2} \quad (22)$$

DEN is defined as

$$DEN = \frac{1 + K_{CO}\,p_{CO} + K_{H_2}\,p_{H_2} + K_{CH_4}\,p_{CH_4} + K_{H_2O}\,p_{H_2O}}{p_{H_2}} \quad (23)$$

where r_i($kmol\,kg_{cat}^{-1}\,h^{-1}$) is the rate of reaction, i. Reaction constants, k_i, can be calculated from the pre-exponential factors using the Arrhenius equation and the Van't Hoff equation. The activation energy, E_i, and adsorption enthalpy of the species, ΔH_j, are taken from a study by Xu and Froment [19]:

$$k_i = A_i \exp\left(-\frac{E_i}{RT}\right) \quad (24)$$

$$K_j = A_j \exp\left(-\frac{\Delta H_j}{RT}\right) \quad (25)$$

Relevant pre-exponential factors, activation energy and equilibrium constants are shown in Tables 2–4, respectively.

Table 3
Adsorption constants

Species	A_i (bar^{-1})	ΔH_i ($kJ\,mol^{-1}$)
CH_4	6.65×10^{-4}	−38.28
CO	8.23×10^{-5}	−70.65
H_2	6.12×10^{-9}	−82.90
H_2O	1.77×10^{-5} bar	88.68

Table 4
Equilibrium constants

Reaction	Equilibrium constant K_{pi}	Unit
1	$5.75 \times 10^{12} \exp(-11476/T)$	bar^2
2	$1.26 \times 10^{-2} \exp(4639/T)$	bar^0
3	$K_{p1}K_{p2}$	bar^2

3.5. Code validation

3.5.1. Cold flow

In this section, a developed code is validated with analytical solutions for micro-channel flow as a benchmark [20]. The SR reaction takes place in a packed bed, which is modelled as porous media. Analysis of fluid flow in porous media must be performed carefully, since the pressure drop is comparably greater than in the regular fluid region. A high pressure drop affects the system efficiency of the steam reformer. As shown in Fig. 5(a), the ideal composite system consists of a porous medium and an overlying fluid layer. When the flow enters the ideal composite system, the normalized velocity profile is compared with the analytical solution in the developed flow region, as presented in Fig. 5(b). The Darcy number in the simulation is 0.001, and continuous

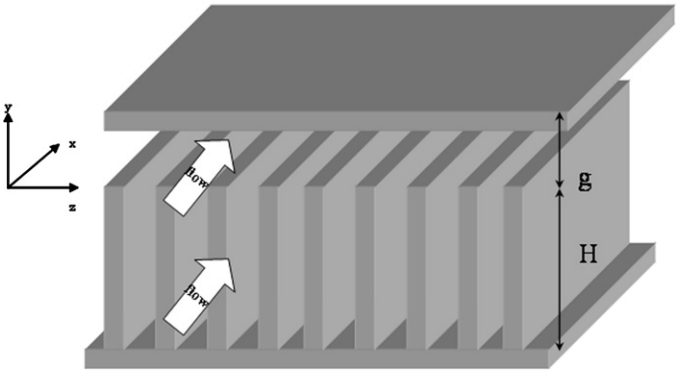

(a)

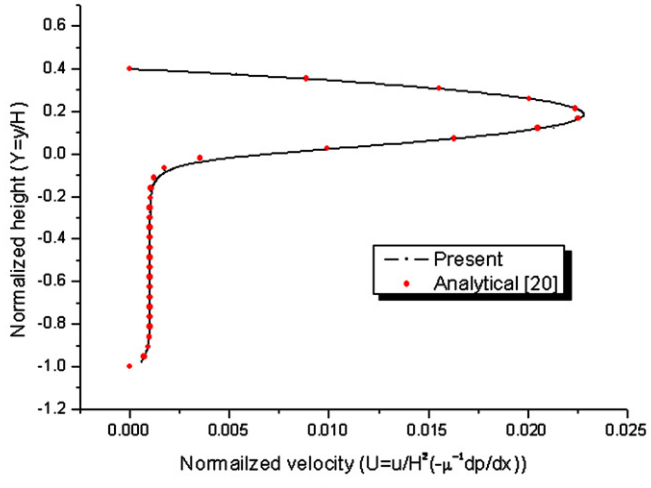

(b)

Fig. 5. (a) Ideal composite system; and (b) comparison between numerical and analytical solution ($\varepsilon = 0.7$).

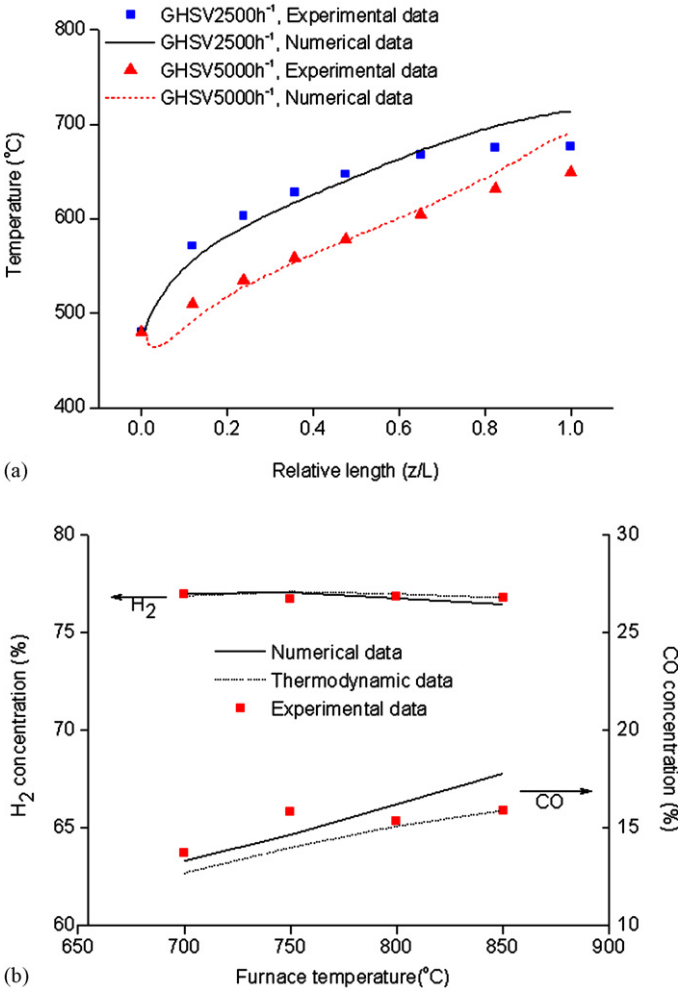

Fig. 6. (a) Comparison of temperature profiles between numerical and experimental results vs. different GHSVs ($T^{in} = 480\,^{\circ}C$, S:C = 3.0). (b) Comparison of selected gas compositions between numerical, thermodynamic, and experimental results vs. different furnace temperatures ($T^{in} = 480\,^{\circ}C$, S:C = 3.0).

velocity and slip shear stress conditions are imposed at the interface between the regular fluid and the porous media. From the results, it can be verified that the developed code predicts the fluid flow in the porous media with adequate accuracy, as shown in Fig. 5(b).

3.5.2. Reacting flow

Using the established model, numerical simulations are carried out (using the same geometry and operating conditions as applied in the experiment) to validate the developed code. Temperature profiles measured from the outer reformer wall are implemented as a thermal boundary condition to compare the results. The data given in Fig. 6(a) and (b) conform that the numerical results are in good agreement with the experimental results.

3.6. Numerical results

In this section, numerical investigations are made of the effects of parameters for operating conditions such as inlet tem-

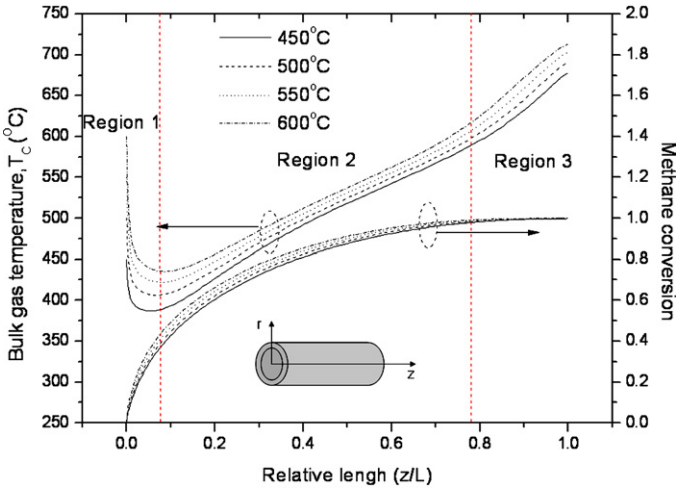

Fig. 7. Bulk gas temperature and methane conversion vs. different inlet gas temperatures (T_w = 800 °C, S:C = 3.0, GHSV = 1000 h^{-1}).

perature, reformer wall temperature, S:C ratio, and GHSV. It is found that high values of inlet gas temperature and reformer wall temperature are favourable. Nevertheless, it is necessary to take energy efficiency into account at high operating temperatures. To investigate the SR reformer numerically, a bench-scale catalyst bed of 6 cm in diameter and 30 cm in length was selected.

To assess the influence of the inlet gas temperature, the reactor wall is maintained at 800 °C the S:C ratio at 3.0, and the GHSV at 1000 h^{-1}. When the inlet gas temperature is higher, the catalyst bed temperature at the centre is also higher (see Fig. 7), which results in higher production of hydrogen and methane conversion. Methane conversion is defined as

$$x = \frac{F^{in}_{CH_4} - F_{CH_4}(z^*)}{F^{in}_{CH_4}} \quad (26)$$

where $F^{in}_{CH_4}$ is the flux of methane at the inlet, and $F_{CH_4}(z^*)$ is the flux of methane at $z = z^*$.

In Fig. 7, the catalyst bed can be classified into three regions—(1) region 1: reaction-dominant region; (2) region 2: mixed reaction and heat transfer region; and (3) region 3: heat-transfer-dominant region. At the entrance region (region 1), the gas mixture enters and SR predominantly takes place, resulting in a decrease in the bulk gas temperature. The heat transfer and SR then occur simultaneously in region 2. Here, the heat transfer is marginally greater than the reaction and therefore the bulk gas temperature continuously increases. Afterwards, in region 3, heat transfer from the wall is dominant, since there is not sufficient fuel to reform, so that the gradient of the temperature profile is steeper than that of region 2.

The influence of the reactor wall temperature was also investigated. The inlet gas temperature is 450 °C, the S:C ratio is 3.0, and GHSV is 3000 h^{-1}, which constitutes a relatively short residence time with this geometry. As an operating parameter, a maximally high reactor wall temperature is also favourable with respect to energy efficiency. The data in Fig. 8 show that the bulk gas temperature behaviour can be clearly distinguished on the

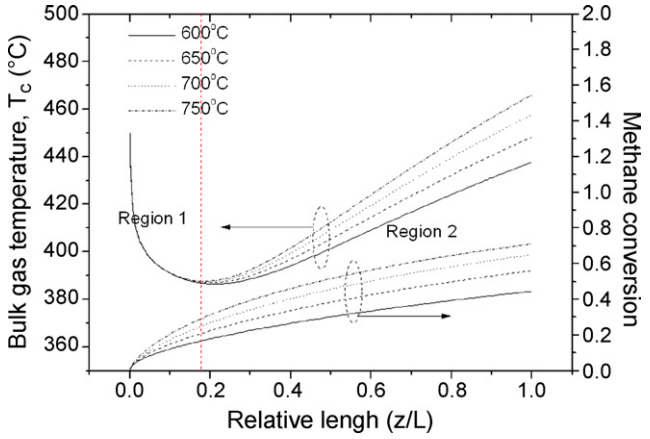

Fig. 8. Bulk gas temperature and methane conversion vs. different reformer wall temperatures (T^{in} = 450 °C, S:C = 3.0, GHSV = 3000 h^{-1}).

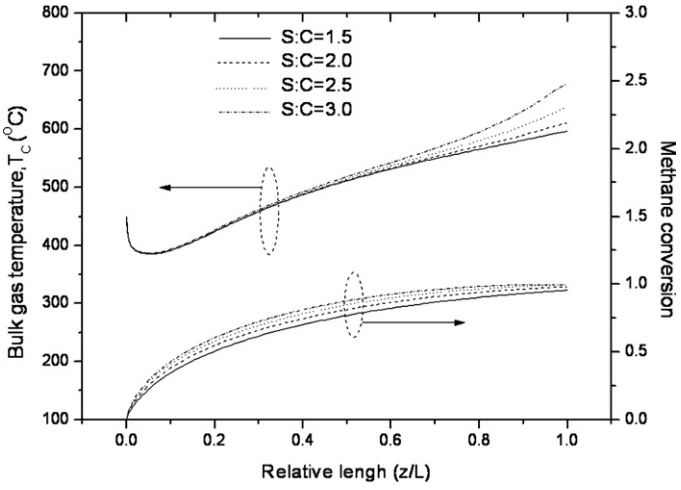

Fig. 9. Bulk gas temperature and methane conversion vs. different S:C ratios (T^{in} = 450 °C, T_w = 800 °C, GHSV = 1000 h^{-1}).

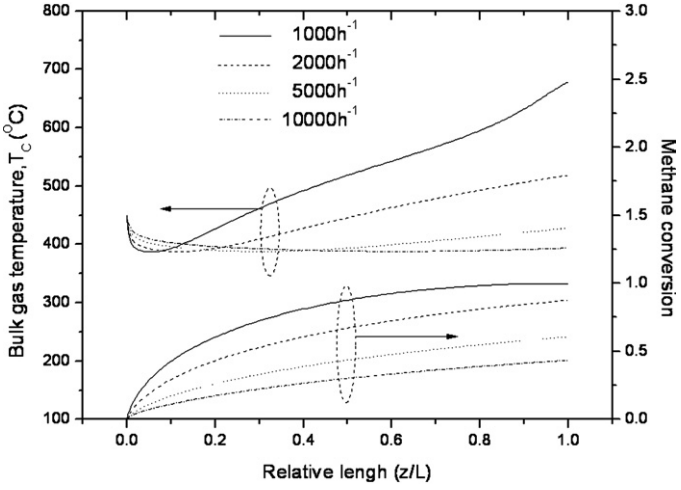

Fig. 10. Bulk gas temperature and methane conversion vs. different GHSVs (T^{in} = 450 °C, T_w = 800 °C, S:C = 3.0).

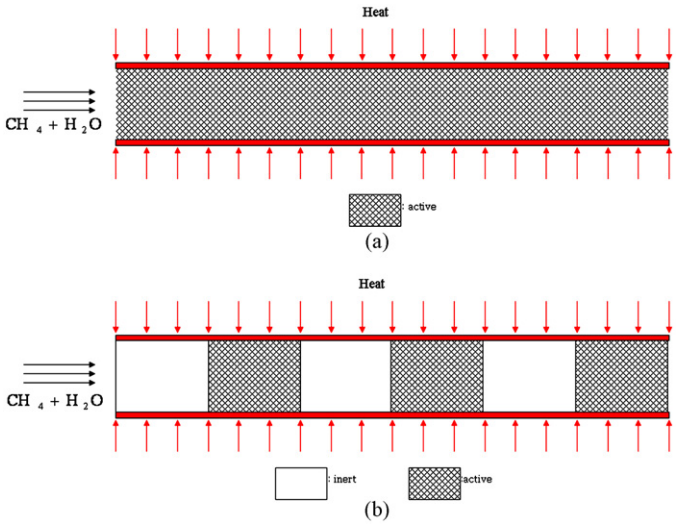

Fig. 11. (a) Typical packing; and (b) mixed packing.

basis of two regions; region 3 as shown in Fig. 7 does not arise due to the relatively higher GHSV.

The effect of S:C ratio when the inlet gas temperature and reformer wall temperature are maintained at 450 and 800 °C, respectively, is presented in Fig. 9. The GHSV is 1000 h^{-1}. As the S:C ratio is increased, methane conversion also increases. An overly high S:C ratio can, however, lead to relatively low hydrogen concentrations according to the chemical equilibrium. Hence, an appropriate range of S:C ratio must be selected.

Finally, the influence of GHSV was examined based on the heat transfer limitation from the reactor wall. The inlet gas temperature and wall temperature were 450 and 800 °C, respectively, and the S:C ratio was 3.0. Methane conversion is found to be remarkably poor when GHSV exceeds 5000 h^{-1}, see Fig. 10. Hence, the GHSV should be carefully selected as regards the residence time of the gas mixture and the effect of heat transfer from the wall to the centre of a given catalyst bed.

4. New method of catalyst packing

In this section, an efficient catalyst packing method is proposed with the aim of enhancing the heat transfer characteristics.

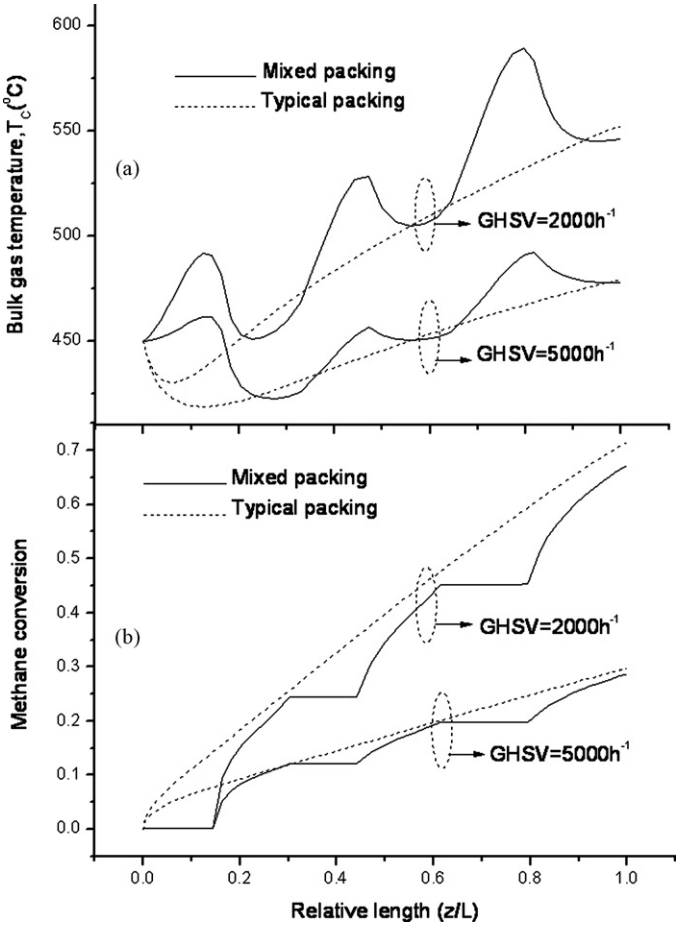

Fig. 12. (a) Bulk gas temperature vs. different packing methods and GHSVs (heat flux: 5 kW m^{-2}, T^{in} = 450 °C, S:C = 3.0); and (b) methane conversion vs. different packing methods and GHSVs (heat flux: 5 kW m^{-2}, T^{in} = 450 °C, S:C = 3.0).

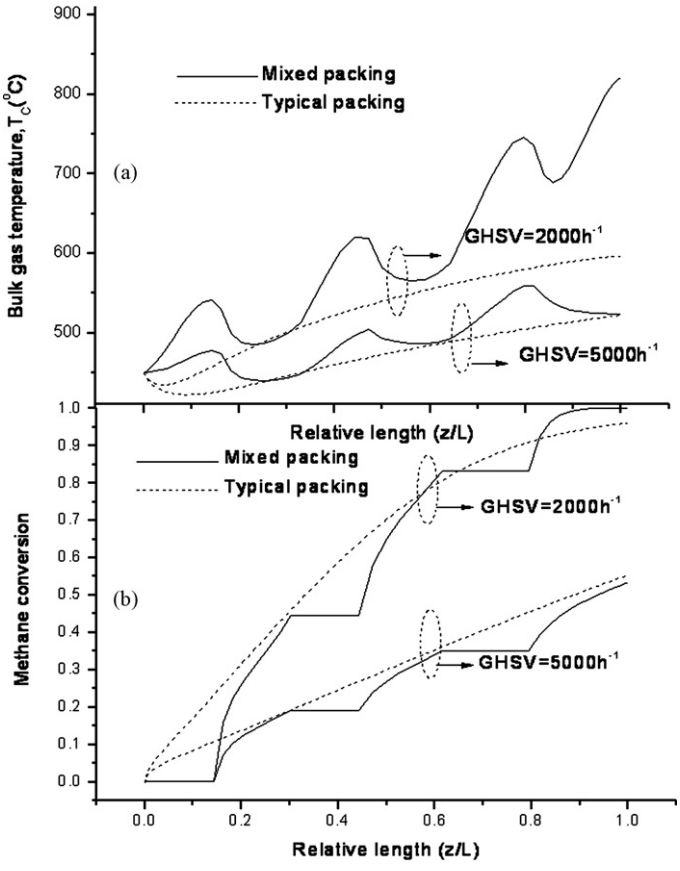

Fig. 13. (a) Bulk gas temperature vs. different packing methods and GHSVs (heat flux: 10 kW m^{-2}, T^{in} = 450 °C, S:C = 3.0); and (b) methane conversion vs. different packing methods and GHSVs (heat flux: 10 kW m^{-2}, T^{in} = 450 °C, S:C = 3.0).

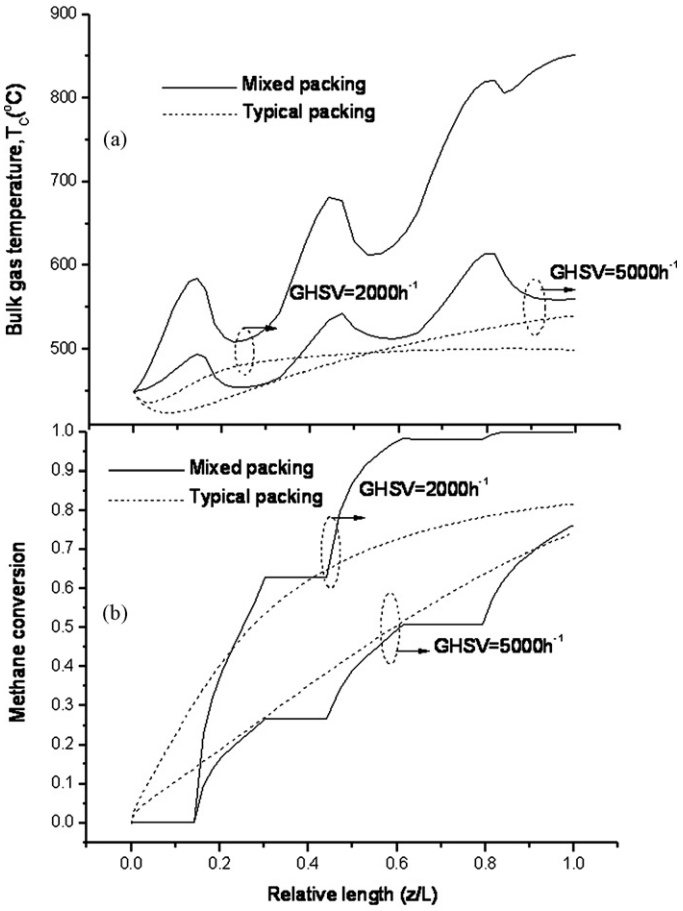

Fig. 14. (a) Bulk gas temperature vs. different packing methods and GHSVs (heat flux: 15 kW m^{-2}, T^{in} = 450 °C, S:C = 3.0); and (b) methane conversion vs. different packing methods and GHSVs (heat flux: 15 kWm^{-2}, T^{in} = 450 °C, S:C = 3.0).

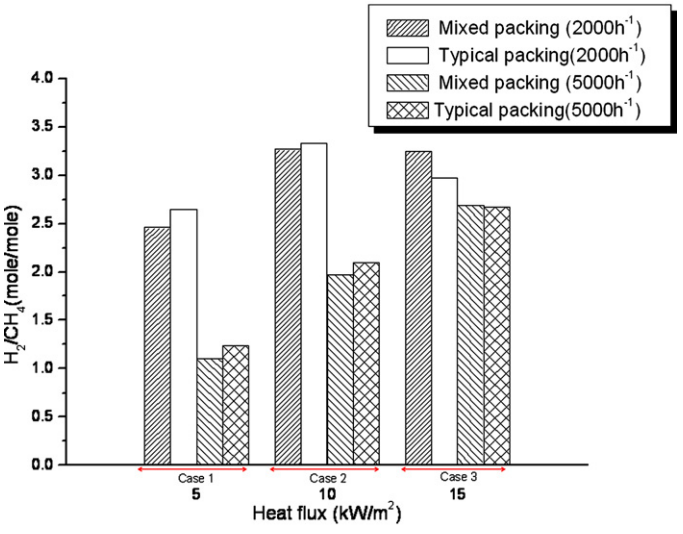

Fig. 15. Hydrogen production to fed methane (mole to mole) vs. different packing methods, GHSVs, and heat fluxes (T^{in} = 450 °C, S:C = 3.0).

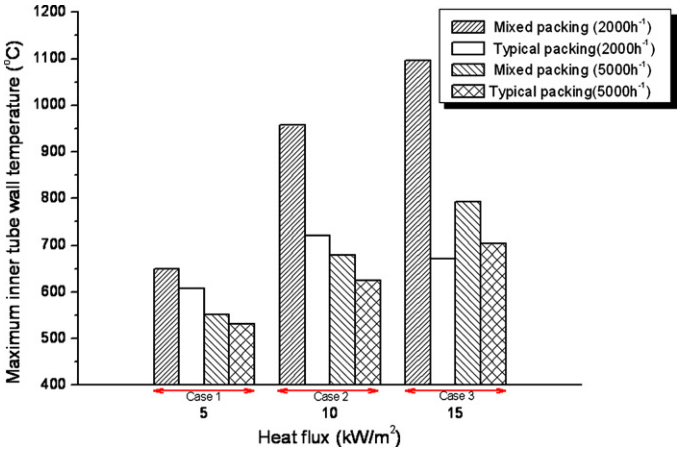

Fig. 16. Maximum inner tube wall temperature vs. different packing methods, GHSVs, and heat fluxes (T^{in} = 450 °C, S:C = 3.0).

Two different catalyst packing configurations are illustrated in Fig. 11, namely, (a) a conventional packing and (b) new configuration to enhance heat transfer and the endothermic reaction.

In the new packing configuration, inert catalysts are inserted between active catalysts in a series to recover heat at the region where heat transfer from the wall occurs and there is no significant endothermic reaction. Thus the gas temperature increases at this region and potentially enhances the desired reaction at the next catalytic region. The performance of this packing method has been extensively compared with typical methods under the same operating conditions. In the new packing approach, catalyst loading is reduced by 50%, which reduces the production cost of the syngas.

In Figs. 12–14, (a) illustrates the bulk gas temperature at the centre of the reactor, whereas (b) gives methane conversion with different heat fluxes and GHSVs. In Fig. 12(a) and (b), the temperature at the reactor centre and the methane conversion are compared when a heat flux of 5 kW m^{-2} is applied. Methane conversion and hydrogen production are similar at both GHSVs, as shown in Figs. 12(a) and 15. Nevertheless, the temperature of the inner tube wall with the new packing approach is maintained at a slightly higher level than that experienced with a typical packing approach, as shown in Fig. 16.

In Fig. 13(a) and (b), more heat is supplied to the reactor. The hydrogen production of the proposed packing configuration is similar to that of a typical packing approach, as shown in Fig. 15. The maximum inner tube wall temperature with the new packing method is remarkably higher at the rear of the bed, because the endothermic reaction is finished at a relatively low GHSV (2000 h^{-1}). In this case, a slightly higher GHSV (5000 h^{-1}) reduces the tube wall temperature (note, the GHSV should be also selected with care in view of hydrogen production). Hydrogen production with respect to the supplied methane at the same GHSV is similar to that for a typical packing configuration, as shown in Fig. 15.

The bulk gas temperature and methane conversion when heat flux of 15 kW m^{-2} is applied are shown in Fig. 14(a) and (b), respectively. For a relatively low GHSV (2000 h^{-1}, case 3), hydrogen production with the new packing method is better than

that obtained with the typical packing method. In the latter, the heat activates the endothermic reaction very strongly near the reactor wall, compared with the other cases (cases 1 and 2). Thus heat cannot penetrate to the centre of the reactor and this results in low methane conversion and hydrogen production. On the other hand, in the relatively high GHSV ($5000\,h^{-1}$) case, hydrogen production is almost the same for the different packing methods. These phenomena result from the relatively low residence time for the reactions in the reformer. Nevertheless, the mixed packing method is still advantageous for economical use of catalyst.

Maximum inner tube wall temperatures for the two different packing methods are given in Fig. 16. When a relatively small amount of heat is applied (case 1), the maximum temperature difference between the two packing methods is quite small so that thermal impact on the reformer tube is virtually the same. On the other hand, material problems could arise in the high heat flux region (cases 2 and 3), as shown in Fig. 16. These problems can be solved by the operating in a relatively higher GHSV region (i.e., $5000\,h^{-1}$ compared with $2000\,h^{-1}$).

5. Conclusion

Steam reforming of methane over nickel alumina has been investigated both experimentally and numerically. Based on the experimental results, a heterogeneous two-dimensional reactor model has been developed and extensively validated. The influence of the operating parameters (e.g., inlet gas temperature, reactor wall temperature S:C ratio and the GHSV) has been examined. It is found that high inlet gas and reactor wall temperatures are favourable, but these parameters have to be selected carefully with respect to energy efficiency. An appropriate S:C ratio should be selected in order to maximize the hydrogen production rate. On the other hand, a high gas flow rate is unfavourable due to the short residence time and the heat transfer limitation. Thus, a moderate GHSV also should be applied. From these results, it is concluded that heat transfer is very significant to obtain higher hydrogen production in a given catalyst bed.

To overcome the heat transfer limitation at moderate and higher flow rates, and thereby improve reactor performance, a new catalyst packing method is proposed. When heat is applied to the reactor, the hydrogen production is almost the same or better than that obtained with a typical packing approach. The proposed catalyst packing method shows good performance and requires a smaller loading of catalyst because heat recovery is carried out in an inert catalyst bed. It should be noted, however, that the reactor tube for the mixed packing method should be carefully designed so as to avoid hot spots.

Acknowledgements

This work was supported by the New & Renewable Energy R&D program (2004-N-HY12-P-01-4-033-2006) under the Korea Ministry of Commerce, Industry and Energy (MOCIE), and was conducted under the Best Lab program of the Ministry of Commence, Industry and Energy (MOCIE).

References

[1] J. Larminie, A. Dicks, Fuel Cell Systems Explained, second ed., John Wiley & Sons, 2003, pp. 229–279.
[2] R. O'Hayre, S.-W. Cha, W. Colella, F.B. Prinz, Fuel Cell Fundamentals, John Wiley & Sons, New York, 2006, pp. 292–306.
[3] S. Rakass, H. Oudghiri-Hassani, P. Rowntree, N. Abatzoglou, J. Power Sources 158 (2006) 485–496.
[4] Y.-S. Seo, D.-J. Seo, Y.-T. Seo, W.-L. Yoon, J. Power Sources 161 (2006) 1208–1216.
[5] C.N. Hamelinck, A.P. Faaij, J. Power Sources 111 (2002) 1–22.
[6] D.L. Stojić, M.P. Marčeta, S.P. Sovilj, Š.S. Miljanić, J. Power Sources 118 (2003) 315–319.
[7] J. Udagawa, P. Aguiar, N.P. Brandon, J. Power Sources 166 (2007) 127–136.
[8] G.E. Voecks, in: W. Vielstich, H.A. Gasteiger, A. Lamm (Eds.), Handbook of Fuel Cells—Fundamentals, Technology and Applications, vol. 3, John Wiley & Sons, 2003, pp. 229–242.
[9] I. Dybkjær, Fuel Process. Technol. 42 (1995) 85–107.
[10] J.P. Rostrop-Nielsen, L.J. Christiansen, J.-H. Bak Hansen, Appl. Catal. 43 (1988) 287–303.
[11] J.P. Rostrup-Nielsen, in: J.R. Anderson, M. Boudard (Eds.), Catalysis Science and Technology, vol. 5, Springer, Berlin, 1984, pp. 14–30.
[12] M.N. Pedernera, J. Piña, D.O. Borio, V. Bucalá, Chem. Eng. J. 94 (2003) 29–40.
[13] J. Piña, N.S. Schbib, V. Bucalá, D.O. Borio, Ind. Eng. Chem. Res. 40 (2001) 5215–5221.
[14] G.F. Froment, K.B. Bishoff, Chemical Reactor Analysis and Design, Wiley, New York, 1979, pp. 451–508.
[15] J. Xu, G.F. Froment, AIChE J. 35 (1989) 97–103.
[16] N. Jeong, D.H. Choi, C.-L. Lin, J. Micromech. Microeng. 16 (2006) 2240–2250.
[17] R.B. Bird, W.E. Stewart, E.N. Lightfoot, Transport Phenomena, vols. 21–28, second ed., John Wiley & Sons, 2002, pp. 274–278.
[18] D.L. Hoang, S.H. Chan, Appl. Catal. A: Gen. 268 (2004) 207–216.
[19] J. Xu, G.F. Froment, AIChE J. 35 (1989) 88–96.
[20] J.Y. Min, S.J. Kim, J. Heat Transf.-Trans. ASME 127 (2005) 648–656.